

UCSF

UC San Francisco Previously Published Works

Title

A viral assembly inhibitor blocks SARS-CoV-2 replication in airway epithelial cells.

Permalink

<https://escholarship.org/uc/item/4gg6b31n>

Journal

Communications Biology, 7(1)

Authors

Du, Li

Deiter, Fred

Bouzidi, Mohamed

et al.

Publication Date

2024-04-22

DOI

10.1038/s42003-024-06130-8

Copyright Information

This work is made available under the terms of a Creative Commons Attribution License, available at <https://creativecommons.org/licenses/by/4.0/>

Peer reviewed

<https://doi.org/10.1038/s42003-024-06130-8>

A viral assembly inhibitor blocks SARS-CoV-2 replication in airway epithelial cells

Check for updates

Li Du^{1,2}, Fred Deiter^{2,3}, Mohamed S. Bouzidi^{1,2}, Jean-Noël Billaud⁴, Graham Simmons^{1,2}, Prerna Dabral^{1,2}, Suganya Selvarajah⁵, Anuradha F. Lingappa⁵, Maya Michon⁵, Shao Feng Yu⁵, Kumar Paulvannan⁵, Balaji Manicassamy⁶, Vishwanath R. Lingappa⁶, Homer Boushey², John R. Greenland^{2,3} & Satish K. Pillai^{1,2} ✉

The ongoing evolution of SARS-CoV-2 to evade vaccines and therapeutics underlines the need for innovative therapies with high genetic barriers to resistance. Therefore, there is pronounced interest in identifying new pharmacological targets in the SARS-CoV-2 viral life cycle. The small molecule PAV-104, identified through a cell-free protein synthesis and assembly screen, was recently shown to target host protein assembly machinery in a manner specific to viral assembly. In this study, we investigate the capacity of PAV-104 to inhibit SARS-CoV-2 replication in human airway epithelial cells (AECs). We show that PAV-104 inhibits >99% of infection with diverse SARS-CoV-2 variants in immortalized AECs, and in primary human AECs cultured at the air-liquid interface (ALI) to represent the lung microenvironment in vivo. Our data demonstrate that PAV-104 inhibits SARS-CoV-2 production without affecting viral entry, mRNA transcription, or protein synthesis. PAV-104 interacts with SARS-CoV-2 nucleocapsid (N) and interferes with its oligomerization, blocking particle assembly. Transcriptomic analysis reveals that PAV-104 reverses SARS-CoV-2 induction of the type-I interferon response and the maturation of nucleoprotein signaling pathway known to support coronavirus replication. Our findings suggest that PAV-104 is a promising therapeutic candidate for COVID-19 with a mechanism of action that is distinct from existing clinical management approaches.

Severe acute respiratory syndrome coronavirus-2 (SARS-CoV-2), the etiological agent of the ongoing COVID-19 pandemic, belongs to a highly contagious betacoronavirus¹. The high transmission and variation of SARS-CoV-2 poses an ongoing threat to global public health. Despite multiple vaccine options, only 65.4% of people are currently fully vaccinated worldwide, due in part to lack of vaccine access as well as behavioral resistance to vaccination. Moreover, many people remain at high risk for severe COVID-19 due to decreased vaccine efficacy and increased risk of respiratory failure associated with immune compromise.

For the treatment of SARS-CoV-2, anti-SARS-CoV-2 monoclonal antibodies (mAbs) that target the spike protein represent one class of therapeutic candidates approved by the FDA for COVID-19 patients^{2,3}. However, the efficacy of anti-SARS-CoV-2 mAbs is negligible in the face of currently circulating viral variants⁴. Beyond mAbs, antiviral small-molecule drugs have been developed that target specific parts of the viral life cycle to prevent infectivity, severe illness, and death attributed to COVID-19. Three

antiviral agents that have been shown to directly inhibit SARS-CoV-2 replication in vitro are currently authorized by the FDA or FDA-granted emergency use authorization (EUA) for the treatment of COVID-19: viral RNA-dependent RNA polymerase (RdRp) inhibitors, remdesivir and molnupiravir⁴⁻⁶, and a viral 3C-like protease inhibitor, paxlovid, which consists of nirmatrelvir and ritonavir⁷. Clinical studies have shown that remdesivir is not associated with statistically significant clinical benefits⁸. In vitro studies have shown that molnupiravir exposure may increase the risk of mutagenesis in the host genome^{9,10}. Paxlovid treatment is often associated with COVID-19 rebound following the treatment cycle¹¹. Taken together, these realities illustrate the need for effective and broad-spectrum antiviral drugs for COVID-19 with minimal off-target effects.

Recent studies have focused on the SARS-CoV-2 viral life cycle to find additional targets for drug therapy, providing candidate SARS-CoV-2 entry and attachment inhibitors^{12,13}, viral protease inhibitors^{14,15}, and N assembly inhibitors that reduce viral nucleocapsid (N)-genome RNA interaction^{16,17}.

¹Vitalant Research Institute, 360 Spear St., San Francisco, CA 94105, USA. ²University of California, San Francisco, CA 94143, USA. ³Veterans Administration Health Care System, 4150 Clement St., San Francisco, CA 94121, USA. ⁴DNAnexus, 1975 W El Camino Real, Mountain View, CA 94040, USA. ⁵Prosetta Biosciences Inc, 670 5th St., San Francisco, CA 94107, USA. ⁶University of Iowa, Iowa City, IA 52242, USA. ✉e-mail: satish.pillai@ucsf.edu

However, data are limited describing agents that selectively inhibit the late stage of the SARS-CoV-2 viral life cycle of particle formation/budding¹⁸. The viral assembly/budding process is a dynamic program dependent on transient multi-protein assembly complexes¹⁹. One approach to identifying these host-viral drug targets is by interrogation of the pathway of viral assembly/budding in cell-free protein synthesis and assembly systems^{20–22}. Small molecules have been identified in this manner that are active against various viral families, including those of rabies virus, HIV-1, and influenza virus^{23–25}.

The small-molecule PAV-104, identified through a moderate-throughput screen involving cell-free protein synthesis and assembly (CFPSA), was recently shown to target host protein assembly machinery in a manner specific to viral assembly²⁴. This compound has minimal host toxicity, and once-daily oral dosing in rats achieves >200-fold of the 90% effective concentration (EC₉₀) in blood. Pharmacokinetic studies of PAV-104 in rats showed a lung-to-plasma ratio of 0.3 after oral administration²⁴. The chemotype shows broad activity against respiratory viral pathogens, including *Orthomyxoviridae*, *Paramyxoviridae*, *Adenoviridae*, *Herpesviridae*, and *Picornaviridae*, with low susceptibility to evolutionary escape.

Here, we evaluated the antiviral effect of PAV-104 against SARS-CoV-2 infection in immortalized and primary human airway epithelial cells (AECs), and elucidated the mechanism underlying this antiviral activity. Our results show that PAV-104 treatment potently inhibits the replication of diverse SARS-CoV-2 variants. We further demonstrate that PAV-104 specifically inhibits the late stages of the SARS-CoV-2 replication cycle, perturbing the oligomerization of viral N, and thereby blocking viral capsid assembly and budding. PAV-104 treatment also reverses SARS-CoV-2 induction of the type-I interferon (IFN) response and the maturation of nucleoprotein signaling pathway, which supports coronavirus replication within the target cell. Together, our data suggest that PAV-104 is a promising therapeutic candidate for COVID-19, and its mechanism of action is distinct from existing clinical strategies.

Results

PAV-104 suppresses SARS-CoV-2 infection in Calu-3 cells

The synthesis and molecular structure of PAV-104 (Fig. 1), a small-molecule drug recently associated with pan-respiratory virus antiviral activity²⁴, is described in detail in the Methods section. To investigate the impact of PAV-104 on SARS-CoV-2 infection, we first determined the cytotoxicity of PAV-104, to optimize dosing in Calu-3 cells. The 50% cytotoxic concentration (CC₅₀) value detected by MTT assay was 1306 nM for PAV-104 in Calu-3 cells (Fig. 2a). Next, we evaluated the effects of PAV-104 on SARS-CoV-2 (USA-WA1/2020) replication at 6.25 nM, 25 nM, 50 nM, and 100 nM concentrations. Calu-3 cells were pretreated for one hour with PAV-104 followed by infection with SARS-CoV-2 at an MOI of 0.01, and PAV-104 was maintained in the media until 24 h following viral infection. SARS-CoV-2 replication, as measured by quantitation of viral nucleocapsid (N) gene expression, was decreased significantly by treatment with PAV-104 in a dose-dependent manner ($p < 0.01$) (Fig. 2b). Similarly, release of infectious virus in the supernatant was suppressed significantly by PAV-104 in a dose-dependent manner, as measured by median tissue culture infectious dose (TCID₅₀) ($p < 0.01$) (Fig. 2c), with up to 75-fold reduction at the highest concentration of PAV-104. The inhibition of virus production by PAV-104 was confirmed by using an immunofluorescence assay (IFA) (Fig. 2d, e). Taken together, these data demonstrate that PAV-104 decreases SARS-CoV-2 viral production in susceptible Calu-3 cells.

PAV-104 inhibits SARS-CoV-2 more potently than remdesivir in Calu-3 cells

Remdesivir is the first approved small-molecule anti-SARS-CoV-2 drug for COVID-19 treatment and shows potent anti-SARS-CoV-2 activity in Calu-3 cells^{26,27}. To compare the anti-SARS-CoV-2 efficacies of PAV-104 with remdesivir in Calu-3 cells, Calu-3 cells were infected with SARS-CoV-2 (USA-WA1/2020) for 48 h at the MOI of 0.001 and treated with varying doses of PAV-104 or remdesivir. Cells and supernatants were harvested for

quantification of N expression by RT-qPCR, and quantification of infectious viral titers by TCID₅₀, respectively. Both compounds displayed dose-dependent inhibition of viral replication (Fig. 3a–d). Remdesivir inhibited SARS-CoV-2 with a mean 90% maximal EC₉₀ value of 219.9 nM, as determined by RT-qPCR measurement of the SARS-CoV-2 N gene (Fig. 3b). PAV-104 was more potent (mean EC₉₀ = 24.5 nM) than remdesivir ($p < 0.0005$) (Fig. 3b). EC₅₀ value determined by quantification of infectious virus in the supernatants showed a similar trend (Fig. 3d). Thus, PAV-104 inhibits SARS-CoV-2 more potently than remdesivir in Calu-3 cells.

PAV-104 is a highly potent antiviral inhibitor of SARS-CoV-2 in primary airway epithelial cells

Upper and lower airways in humans are known to be the first gateway for SARS-CoV-2 infection²⁸. To investigate the antiviral activity of PAV-104 against SARS-CoV-2 in human primary AECs, we performed antiviral assays in air/liquid interface (ALI)-cultured AECs, which is useful in modeling the in vivo effects of PAV-104 on SARS-CoV-2 infection ex vivo²⁹. We pretreated primary AECs from three healthy donors with PAV-104 and then infected them with the SARS-CoV-2 Gamma variant (Pango lineage designation P.1) for 36 h. In PAV-104-treated, SARS-CoV-2-infected AECs cultures, there was >99% inhibition of infection with PAV-104 treatment at the highest tested concentration ($p < 0.01$) (Fig. 4a). We also tested the antiviral effect of PAV-104 on the Delta and Omicron SARS-CoV-2 variants in AECs. Administration of PAV-104 also significantly reduced Delta and Omicron replication in primary AECs ($p < 0.01$) (Fig. 4b). Together, these data demonstrate that PAV-104 exerts potent antiviral activity against a broad range of SARS-CoV-2 variants in primary AECs.

PAV-104 interferes with post-entry steps of the SARS-CoV-2 life cycle

Since PAV-104 was identified based on the inhibition of the viral particle assembly/budding process, we next sought to determine whether PAV-104 inhibits SARS-CoV-2 replication by acting on a post-entry step of the SARS-CoV-2 viral replication cycle as expected. We detected the effect of PAV-104 on SARS-CoV-2 entry by using VSV-SARS-CoV-2 spike-ΔG-luciferase reporter pseudovirus (hereafter referred to as SARS-2-S). Positive serum (P serum), which was predetermined to possess SARS-CoV-2 neutralizing activity, potently reduced SARS-2-S infection ($p < 0.0001$) but did not suppress the infection of VSV-spike G glycoprotein-luciferase reporter pseudovirus (hereafter referred to as VSV-G). PAV-104 showed no effect on SARS-2-S infection or VSV-G infection, indicating that PAV-104 has no effect on SARS-CoV-2 entry (Fig. 5a). To further clarify the stage of the virus replication cycle targeted by PAV-104, we infected Calu-3 cells with SARS-CoV-2 (USA-WA1/2020, MOI = 0.01), and administered PAV-104 at different time points to enable specific assessment of drug effects on viral entry/attachment (early), and post-entry (late) stages of the viral life cycle, using established experimental timelines^{30–32} (Fig. 5b). Our data showed that PAV-104 does not inhibit SARS-CoV-2 infection in the 1 h incubation assay, or the pre-infection treatment condition (Fig. 5c), indicating that PAV-104 does not act on SARS-CoV-2 attachment or entry. Post-infection treatment with PAV-104 did strikingly reduce SARS-CoV-2 viral titer in the supernatant as represented by TCID₅₀ ($p < 0.01$), as compared to post infection treatment with DMSO (negative control) or pre-infection treatment with PAV-104 (Fig. 5c). Consistent with these data, SARS-CoV-2 replication in primary AECs was decreased significantly by treatment with PAV-104 in the post infection condition, but not in the pre-infection treatment scenario ($p < 0.05$) (Fig. 5d). These results suggest that PAV-104 activity can be entirely attributed to blocking the late stage of the SARS-CoV-2 viral life cycle after viral entry.

PAV-104 blocks SARS-CoV-2 viral particle formation

Transient coexpression of four SARS-CoV-2 structural proteins (N, M, E, and S) in cell culture has been shown to produce assembling virus-like particles (VLPs), which can be used to study the viral life cycle such as

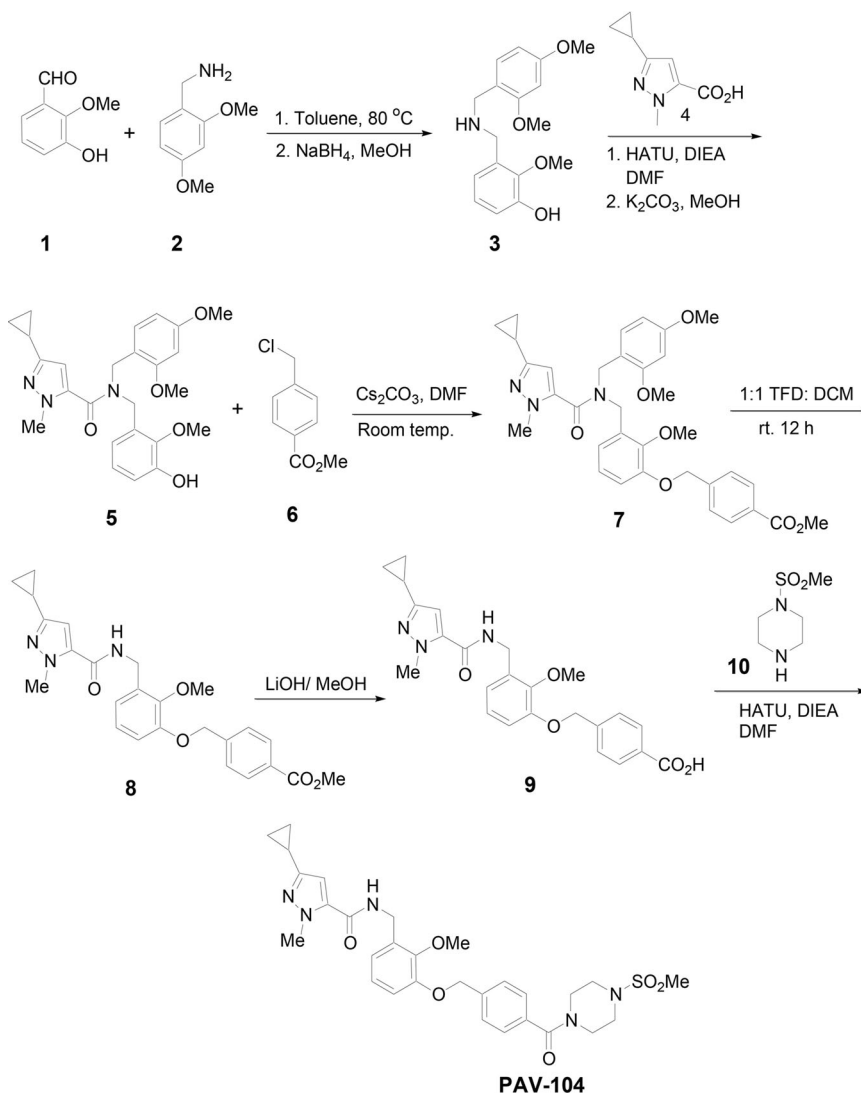


Fig. 1 | Synthesis and molecular structure of PAV-104. To a solution of aldehyde 1 (10 g, 65.79 mmol, 1.0 eq) in toluene was added 2,4-dimethoxybenzyl amine 2 (10.99 g, 65.79 mmol, 1.0 eq), and the reaction mixture was heated at 80 °C for 24 h. Solvent was removed, and the residue was taken in MeOH and cooled using an ice bath. Then sodium borohydride (4.97 g, 131.58 mmol, 2.0 eq) was added slowly, and the reaction mixture was stirred at room temperature for 12 h. Solvent was removed, and the residue was taken in ethyl acetate and then sat. NaHCO₃ was added and stirred for 1 h. The organic layer was separated, dried (MgSO₄), and the solvent was removed to give amine 3, which was used in the next step without further purification. To a solution of the crude amine 3 (5.0 g, 19.1 mmol, 1.0 eq) in DMF (25 mL) was added acid 4 (3.17 g, 19.1 mmol, 1.0 eq), HATU (8.7 g, 22.92 mmol, 1.2 eq.), and DIEA (12.32 g, 95.5 mmol, 5.0 eq) and the reaction mixture was stirred at room temperature for 12 h. The reaction mixture was then diluted with ethyl acetate (EtOAc) and washed with 10% aqueous HCl (1×), sat. NaHCO₃ (1×) and water (3×). Organic layer was collected, dried (MgSO₄), and evaporated to give a residue, which was taken in MeOH, and then K₂CO₃ (2.64 g, 19.1 mmol, 1.0 eq) was added and stirred at room temperature for 12 h. Solvent was removed, and the residue was taken in Ethyl acetate and washed with 10% HCl (1×). Organic layer was separated, dried, and solvent was removed to give a residue, which was purified by column chromatography (EtOAc/ Hexane) to give compound 5. To a stirred solution of compound 5 (1.0 g, 2.22 mmol, 1.0 eq) and cesium carbonate

(1.08 g, 3.33 mmol, 1.5 eq) in DMF (15 mL) was added methyl 4-(chloromethyl) benzoate 6 (450 mg, 2.44 mmol, 1.2 eq) and the reaction mixture was stirred at room temperature for 18 h. The reaction mixture was diluted with ethyl acetate and washed with water (3×). Organic layer was dried and concentrated to give crude product 7. The crude compound 7 was stirred in a 1:1 mixture of TFA: DCM for 12 h. Concentration followed by chromatography purification (Hexane/EtOAc) provided compound 8. To a stirred solution of compound 8 (0.84 mmol, 1.0 eq) in 3:1 mixture of THF: H₂O (12 mL) was added LiOH (40 mg, 1.68 mmol, 2.0 eq) and the reaction mixture was stirred at 65 °C for 12 h. The reaction mixture was evaporated under vacuum to give a residue, which was stirred in a mixture of 10% aqueous HCl and ethyl acetate for 30 min. Organic layer was collected, washed (H₂O, 1×), dried, and concentrated to give crude acid 9. To a solution of the amine 10 (68 mg, 0.552 mmol, 1.2 eq) in DMF (25 mL) were added acid 9 (200 mg, 0.46 mmol, 1.0 eq), HATU (210 mg, 0.552 mmol, 1.2 eq.) and DIEA (0.300 mg, 2.3 mmol, 5.0 eq). The reaction mixture was stirred at room temperature for 12 h. The reaction mixture was then diluted with EtOAc and washed with 10% aqueous HCl (1×), sat. NaHCO₃ (1×) and water (3×). The organic layer was collected, dried (MgSO₄), and evaporated to give a residue, which was purified by column chromatography (EtOAc/ Hexane) to give PAV-104. PAV-104 was dissolved in DMSO.

assembly/budding, egress, and entry^{33,34}. To explore whether PAV-104 results in the inhibition of SARS-CoV-2 viral formation/budding, we quantified production of SARS-CoV-2 structural proteins in VLPs from cell culture supernatants of transfected HEK-293T cells treated with PAV-104 or DMSO. Viral assembly was quantified by western blot and nanoparticle

tracking analysis (NTA) of extracellular vesicles and viral particles. Western blots were performed on proteins from the pellet after ultracentrifugation of transfected cell lysates and culture supernatants. PAV-104 significantly reduced structural protein production in the pellet collected from cell supernatants in a dose-dependent manner ($p < 0.01$), but did not inhibit

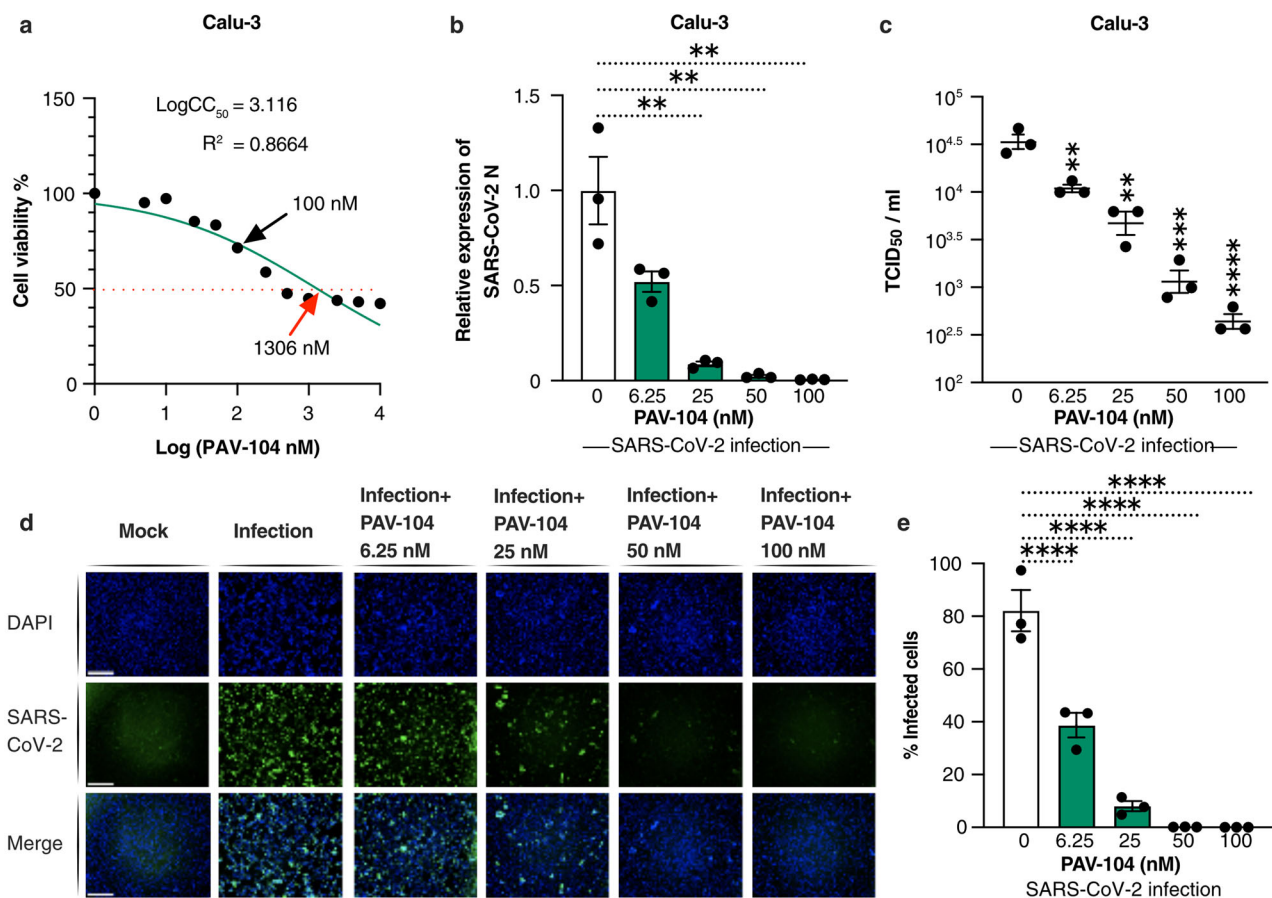


Fig. 2 | PAV-104 decreases virus production in SARS-CoV-2-infected Calu-3 cells. **a** MTT assay was performed on Calu-3 cells to examine the cellular toxicity of PAV-104. Relative cell viability was displayed based on the PAV-104-untreated control (set at 100%). The concentration of 100 nM of PAV-104 is represented by the black arrow. The red arrow represents the CC₅₀ value (1306 nM) of PAV-104. **b** Anti-SARS-CoV-2 activity of PAV-104 in Calu-3 cells was measured by RT-qPCR targeting the N genes. Cells were pretreated with PAV-104 at the indicated concentrations for 1 h, followed by infection with SARS-CoV-2 (USA-WA1/2020, MOI = 0.01) for 24 h in the presence of PAV-104. RNA isolation and RT-qPCR assay were performed 24 h post infection. Data were normalized to the DMSO negative

control. **c** The SARS-CoV-2 titer (TCID₅₀) was measured after treatment with varying doses of PAV-104 as described in **b**. **d** Immunofluorescence staining of Calu-3 cells with DAPI (blue) was performed at 72 h post infection. Cells were pretreated with PAV-104 at the indicated concentrations, followed by infection with SARS-CoV-2 virus. Scale bar, 500 μm. **e** Quantification of SARS-CoV-2 (USA-WA1/2020, MOI = 0.01) infected Calu-3 (FITC-positive) cells (shown in **d**). Data are representative of the results of three independent experiments (*n* = 3 biologically independent samples, mean ± standard error of mean (SEM)). Statistical significance was analyzed by *t* test. *p* ≤ 0.05 [*], *p* ≤ 0.01 [**], *p* ≤ 0.001 [***], *p* ≤ 0.0001 [****].

structural protein synthesis and steady-state levels of actin in the cell lysates (Fig. 6a–c). Consistent with western blot data (Fig. 6a), our NTA results showed that cells transfected with the four SARS-CoV-2 structural proteins displayed increased nanoparticle production as compared to cells transfected with empty vectors (*p* < 0.001) (Fig. 6d), reflecting production and release of SARS-CoV-2 VLPs. PAV-104 treatment inhibited the concentration of nanoparticles in the supernatants of cells transfected with the four SARS-CoV-2 structural proteins in a dose-dependent manner (*p* < 0.01) (Fig. 6d), while no effect on nanoparticle secretion in empty vector-transfected cell supernatants was observed (suggesting that extracellular vesicle secretion is not affected by PAV-104). These data indicate that PAV-104 specifically inhibits VLP production in our model.

To further investigate the role of PAV-104 on viral particle formation, we infected Calu-3 cells with single-cycle infectious SARS-CoV-2 virus (hereafter referred to as ΔS-VRP) and treated cells with PAV-104. Our data show that PAV-104 does not affect ΔS-VRP N mRNA level (Fig. 7a) or protein synthesis (Fig. 7b, c). However, PAV-104 did significantly inhibit the concentration of viral particles released into the supernatant (Fig. 7d). These data confirm that PAV-104 has no effect on protein synthesis, and blocks SARS-CoV-2 replication specifically through targeting the viral assembly/budding process.

PAV-104 inhibits the oligomerization of the SARS-CoV-2 N

To investigate the main drug target of PAV-104 involved in the SARS-CoV-2 viral particle assembly/budding process, drug resin affinity chromatography (DRAC) was performed²⁴. PAV-104 was coupled to the 4% crosslinked agarose resin²⁴. Cellular extracts from Calu-3 cells with or without SARS-CoV-2 infection were incubated on the PAV-104 drug resin columns with or without PAV-104 covalently attached, allowing the target to bind. After washing, specifically bound material was eluted with free drug (PAV-104), followed by stripping of the remaining bound material from the drug and control columns with 1% SDS. Based on western blotting with an anti-SARS-CoV-2 N antibody, negligible SARS-CoV-2 N was bound to or eluted from control columns to which infected lysates were applied, while abundant SARS-CoV-2 N was bound to and eluted from columns of PAV-104 attached to resin (Fig. 8a), indicating that SARS-CoV-2 N is a major component of the target multi-protein complex. No N reactivity was observed in columns loaded with uninfected lysates as expected. The oligomerization of SARS-CoV-2 N has been demonstrated to be responsible for helping virus envelope formation and particle assembly^{35–37}. To determine if PAV-104 affects the oligomerization of SARS-CoV-2 N to inhibit SARS-CoV-2 viral particle assembly, cells were transfected with N in the presence or absence of PAV-104, followed by analysis with glycerol gradient ultracentrifugation

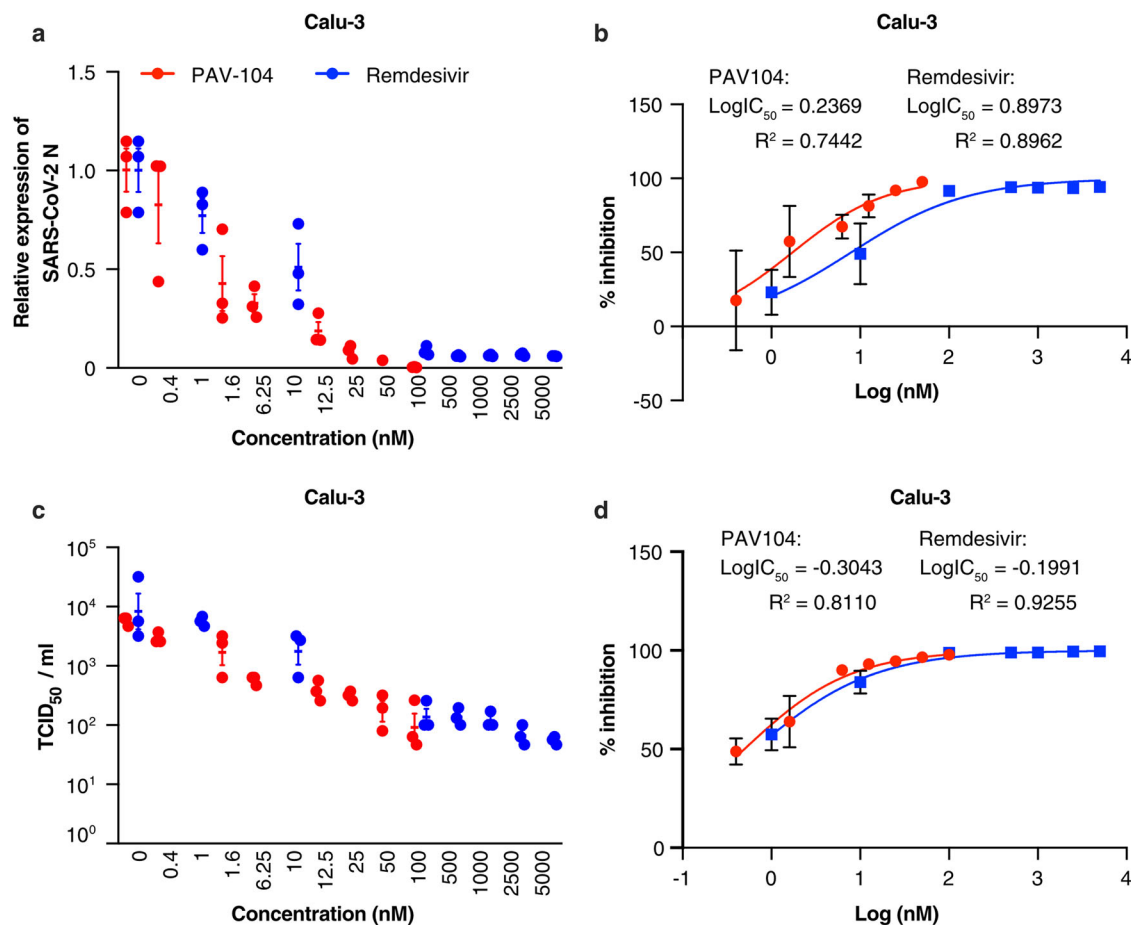


Fig. 3 | PAV-104 inhibits SARS-CoV-2 replication in Calu-3 cells more potently than remdesivir. **a** Reduction of SARS-CoV-2 replication by PAV-104 and remdesivir in Calu-3 cells, as determined by RT-qPCR targeting the N gene. Calu-3 cells were pretreated with DMSO, PAV-104, or remdesivir for one hour, then infected with SARS-CoV-2 at an MOI of 0.001. Cells were collected at 48 hpi. **b** Percent inhibition of SARS-CoV-2 replication by PAV-104 and remdesivir in Calu-3 cells, as determined by RT-qPCR (PAV-104: $\text{EC}_{50} = 1.725$ nM, $\text{EC}_{90} = 24.5$ nM; remdesivir: $\text{EC}_{50} = 7.9$ nM, $\text{EC}_{90} = 219.9$ nM). **c** Reduction of SARS-CoV-2

replication by PAV-104 and remdesivir in Calu-3 cells, as determined by infectious viral titer in the supernatant at 48 hpi. **d** Percent inhibition of SARS-CoV-2 replication by PAV-104 and remdesivir in Calu-3 cells, as determined by infectious viral titer (PAV-104: $\text{EC}_{50} = 0.5$ nM, $\text{EC}_{90} = 10.3$ nM; remdesivir: $\text{EC}_{50} = 0.65$ nM, $\text{EC}_{90} = 19.3$ nM). Data are representative of the results of three independent experiments ($n = 3$ biologically independent samples, mean \pm SEM). Statistical significance was determined by *t* test. $p \leq 0.05$ [*], $p \leq 0.01$ [**], $p \leq 0.001$ [***], $p \leq 0.0001$ [****].

and a commercial ELISA kit to determine N concentrations in fractions. N-expressing cells treated with PAV-104 showed that there is a reduction of the N intermediate complex (Fraction 20–22) as compared to DMSO treatment (Fig. 8b), indicating that the oligomerization of SARS-CoV-2 N is inhibited by PAV-104 treatment. These data support a model in which PAV-104 directly or indirectly affects the oligomerization of SARS-CoV-2 N to inhibit viral particle formation/assembly.

PAV-104 treatment suppresses the IFN signaling and maturation of nucleoprotein gene expression pathways

Finally, to understand the transcriptional impact of PAV-104 in the setting of SARS-CoV-2 infection and immunopathology, we performed RNA-seq analysis on ALI-cultured primary AECs from five different healthy donors infected for 36 h with SARS-CoV-2 (MOI = 0.1) in the presence or absence of PAV-104. Uninfected, untreated cells (Control) were characterized as a reference for both experimental conditions. The effects of PAV-104 administration alone (in the absence of SARS-CoV-2 infection) were evaluated in three additional donors (Supplementary Fig. 1). Differentially expressed gene (DEG) analysis showed that 81 genes were significantly upregulated by SARS-CoV-2 infection alone (Fig. 9a, Supplementary Data 1), with most of them being IFN-related genes, such as OAS3, HELZ2, IFIT3, OAS1, and ISG15. SARS-CoV-2 infection in the presence of PAV-104 exhibited a dramatic impact on the host transcriptome when compared

to uninfected control, with 10,255 DEGs identified (Fig. 9b, Supplementary Data 2), including 5843 downregulated and 4412 upregulated genes. In addition, when compared with SARS-CoV-2 infection alone, SARS-CoV-2 infection in the presence of PAV-104 exhibited a distinct transcriptomic signature, with 9,319 DEGs identified (Fig. 9c, Supplementary Data 3). We additionally examined the impact of PAV-104 treatment on SARS-CoV-2 mRNA levels in the spreading infection by aligning sequencing reads against the SARS-CoV-2 reference genome. The number of reads mapping to each region of the viral genome was calculated and interpreted to infer viral expression patterns (Fig. 9d)²⁹. Consistent with the antiviral effect of PAV-104, the mRNA levels of SARS-CoV-2 were profoundly reduced in the presence of PAV-104. These results confirm the highly potent antiviral activity of PAV-104 against SARS-CoV-2.

Fifteen genes that were significantly upregulated by SARS-CoV-2 infection were significantly down-regulated in the SARS-CoV-2 infection with PAV-104 treatment group: CXCL11, CXCL9, IFIT2, IFIT3, DDX58, SAMD9L, OAS2, IFI44, USP18, SAMD9, DDX60, HERC6, XAF1, RSAD2, XAF1M, DDX60L. Most of these genes are IFN-stimulated genes (ISGs) (Fig. 9e). Gene set enrichment analysis (GSEA) using Reactome database pathway definitions presents a counteracting pattern between the SARS-CoV-2 infection group and the PAV-104 treated group, suggesting that PAV-104 could reverse the viral infection-regulated pathways (Fig. 9f). GSEA revealed that the IFN signaling pathway was the most upregulated

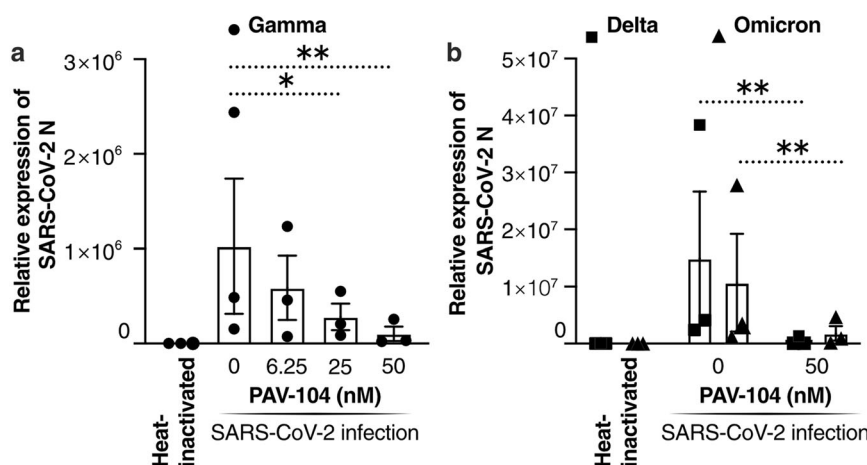


Fig. 4 | PAV-104 inhibits the replication of SARS-CoV-2 variants in human primary airway epithelial cells. **a** Antiviral activity of PAV-104 against SARS-CoV-2 in primary AECs, as determined by RT-qPCR. ALI-cultured primary AECs were pre-incubated with DMSO or PAV-104 at indicated concentrations for one hour and were then infected with heat-inactivated virus and SARS-CoV-2 (lineage P.1, MOI = 0.1) at the apical and basal compartment for two hours. Cells were then washed and supplemented with fresh media containing DMSO or PAV-104. Cells

were collected for RNA isolation and RT-qPCR at 36 hpi. Each color represents data from one donor. **b** Antiviral activity of PAV-104 against SARS-CoV-2 variants (Delta and Omicron) in primary AECs, as determined by RT-qPCR. Each dot represents data from one donor. Data are representative of the results of three independent experiments ($n = 3$ biologically independent samples, mean \pm SEM). Statistical significance was analyzed by paired t tests. $p \leq 0.05$ [*], $p \leq 0.01$ [**], $p \leq 0.001$ [***], $p \leq 0.0001$ [****].

pathway by SARS-CoV-2 infection (Fig. 9f, Supplementary Data 4). Virus-induced IFN signaling was reversed by PAV-104 treatment. The regulation of genes involved in the IFN signaling pathway is shown in Supplementary Fig. 2a, and the modulation of select ISGs was verified by RT-qPCR (Supplementary Fig. 2b).

Of particular interest in our transcriptomic data is the set of genes related to the maturation of nucleoprotein pathway that are selectively upregulated by SARS-CoV-2 infection but not by SARS-CoV-2 infection with PAV-104 treatment (Fig. 9f). SARS-CoV-2 nucleoprotein is found in the host cell cytosol, the nucleus and plasma membrane³⁸. The maturation of nucleoprotein signaling pathway, including oligomerization, ADP-ribosylation, phosphorylation, sumoylation, methylation, and other post-translational modifications of nucleoprotein, is responsible for N movement, interaction with genomic RNAs, interaction with other proteins, and viral particle assembly^{17,39–41}. The regulation of all genes that are involved in the SARS-CoV-2 maturation of nucleoprotein pathway (as defined in the Reactome database) is shown in Supplementary Fig. 2c, and the modulation of select pathway genes was verified by RT-qPCR (Supplementary Fig. 2d). SARS-CoV-2 infection increased the expression of the PARP9, PARP14, and PARP10 genes, but SARS-CoV-2 infection in the presence of PAV-104 treatment down-regulated the expression of these genes (as compared to untreated/uninfected control). Beyond host factors defined by Reactome as members of the maturation of nucleoprotein pathway, PIAS1, and SRPK3, which have been reported to play roles in SUMOylating⁴² and phosphorylating SARS-CoV-2 N⁴³, respectively, were significantly down-regulated in the SARS-CoV-2 infection with PAV-104 treatment group (Supplementary Fig. 2c). The protein arginine methyltransferase (PRMT) 5, 6, 7, and 9 genes were significantly down-regulated by PAV-104 treatment, and members of the PRMT family are known to methylate N¹⁷. Lastly, G3BP1, down-regulated by PAV-104 treatment, is known to be sequestered by SARS-CoV-2 N, leading to suppression of the host immune response to favor virus replication⁴⁴.

Further unsupervised analysis of the gene expression data revealed four distinct clusters (Supplementary Fig. 3a). Gene Ontology (GO) analysis demonstrated that SARS-CoV-2 induction of genes associated with the IFN signaling and response to chemokine pathways was reversed by PAV-104 treatment (cluster 2) (Supplementary Fig. 3b). Genes associated with negative regulation of inclusion body assembly and protein refolding signaling pathways were induced by PAV-104 treatment (cluster 3)

(Supplementary Fig. 3b). Taken together, our findings demonstrate that PAV-104 modulates a diverse repertoire of host factors that are reported to be key players in the trafficking and post-translation modifications of SARS-CoV-2 N that are critical to SARS-CoV-2 maturation and immune evasion.

Discussion

The rapid emergence and spreading of the SARS-CoV-2 Omicron variant that evades many monoclonal antibody therapies illustrates the need for antiviral treatments with low susceptibility to evolutionary escape. Capsid assembly is an essential step in the viral life cycle mediated by the interaction of viral capsid proteins. Inhibition of this process can be used as a therapeutic approach; any proteins, any modifications, or any interactions that participate in or stabilize viral particle assembly in the producer cell can be manipulated to inhibit assembly, prevent release, and protect as-yet-uninfected target cells from subsequent infection.

In our prior work, we identified three small molecules, PAV-431, PAV-471, and PAV-104, as inhibitors of influenza virus assembly using our cell-free protein synthesis and viral assembly screening system²⁴. We further demonstrated that PAV-104, in particular, exerted highly potent antiviral effects against Nipah virus with minimal toxicity²⁴. Here, building on these observations, we investigated the capacity of PAV-104 to inhibit SARS-CoV-2 infection. Our results show that PAV-104 inhibits SARS-CoV-2 replication in AECs, exhibiting potent antiviral effects against multiple viral variants.

We have established that PAV-104 interferes with a post-entry step of the SARS-CoV-2 life cycle and blocks SARS-CoV-2 viral particle assembly/budding based on the following observations: (1) the chemotype of PAV-104 investigated here has no effects on early viral life cycle events (e.g., viral entry), (2) PAV-104 reduces virus release into the cell culture supernatant, (3) PAV-104 treatment does not reduce steady-state levels of cellular proteins and does not impede the translation of viral structural proteins, and (4) PAV-104 interacts with SARS-CoV-2 N and interferes with its oligomerization. Dimerization and oligomerization of SARS-CoV-2 N proteins are essential to enable associations with viral genomic RNA and other viral structural proteins (M, E, and S), playing a critical role in virus particle assembly^{37,45}. In addition to viral particle assembly, the coronavirus N is required for viral mRNA and genome synthesis, viral core formation, and virus budding/envelope formation⁴⁶. Given that some compounds that perturb capsid assembly can result in formation of noninfectious virions⁴⁷,

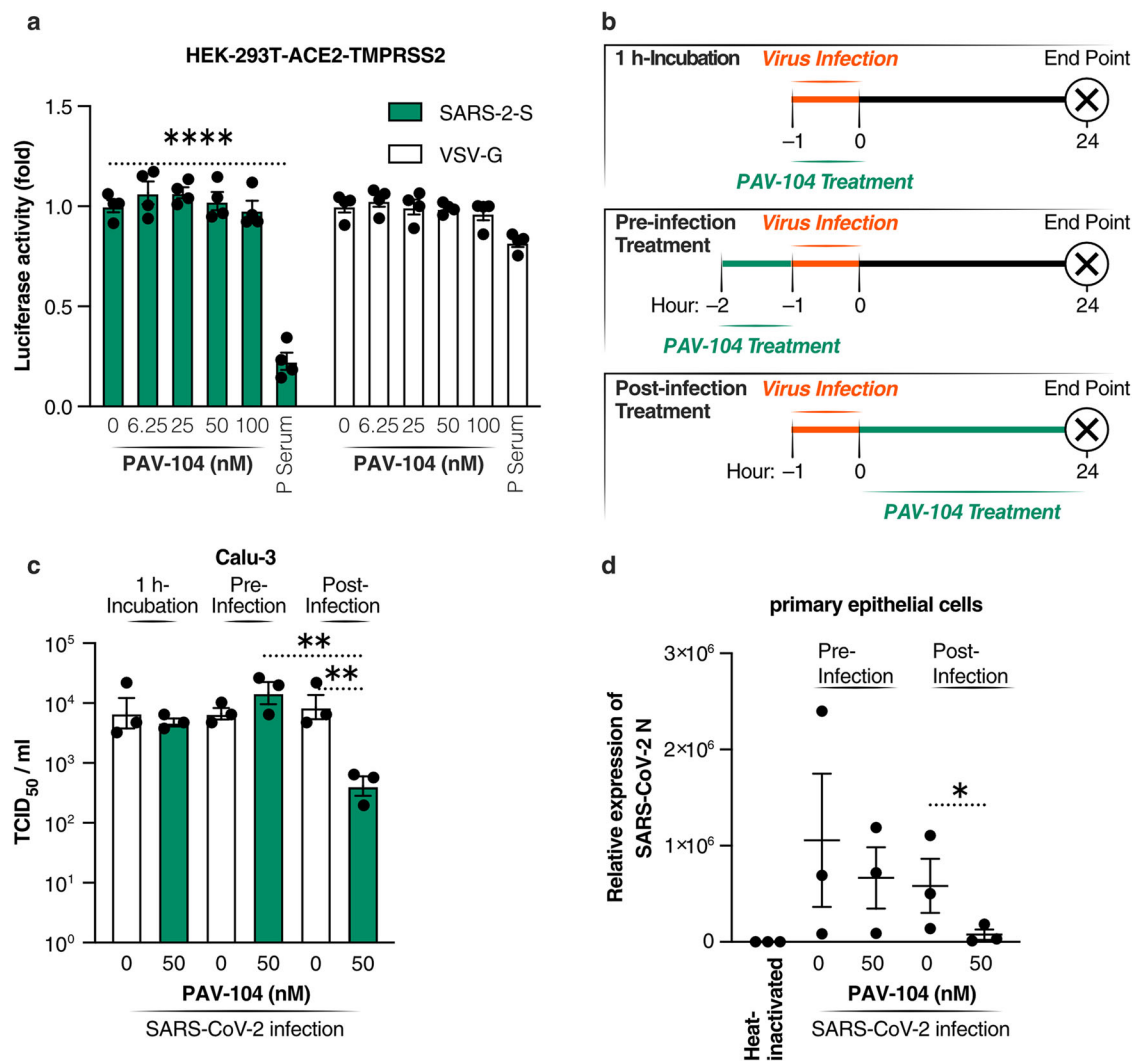


Fig. 5 | PAV-104 inhibits SARS-CoV-2 replication at a post-entry step of the viral life cycle. **a** Relative infectivity of SARS-2-S pseudotyped virus and VSV-G pseudotyped virus in HEK-293T cells overexpressing the ACE2 and TMPRSS2 receptors (HEK293T-ACE2-TMPRSS2) treated with PAV-104 at the indicated concentrations. HEK293T-ACE2-TMPRSS2 cells were exposed to PAV-104 for 1 h and then infected with SARS-2-S pseudotyped virus or VSV-G pseudotyped virus. Pseudotyped viral entry was analyzed by luciferase activity 24 hpi. Positive serum pre-determined to possess anti-SARS-CoV-2 neutralizing activity was used as a positive control. Luciferase signals obtained in the absence of PAV-104 were used for normalization. $n = 4$ biologically independent samples. **b** Schematic timeline of PAV-

104 treatment in Calu-3 cells. Calu-3 cells were incubated with PAV-104 or infected with SARS-CoV-2 at indicated time points as the diagram shows. **c** Virus production (measured as viral titer) in Calu-3 cells treated with PAV-104 at indicated doses and time points. $n = 3$ biologically independent samples. **d** Virus production (measured as viral N gene expression by RT-qPCR) in primary AECs treated with PAV-104 at indicated doses and time points. Heat-inactivated SARS-Cov-2 treatment was used for normalization. $n = 3$ biologically independent samples. Data are representative of the results as mean \pm SEM. Statistical significance was analyzed by t test or paired t test. $p \leq 0.05$ [*], $p \leq 0.01$ [**], $p \leq 0.001$ [***], $p \leq 0.0001$ [****].

PAV-104 effects could potentially extend beyond viral assembly/budding and attenuate the infectivity of SARS-CoV-2, further enhancing its antiviral activity.

Previously, we showed that PAV-104 bound a small subset of the known allosteric modulator 14-3-3, itself implicated in the interactome of SARS-CoV-2^{24,48,49}. Binding of phosphorylated SARS-CoV N to the host 14-3-3 protein in the cytoplasm was reported to regulate nucleocytoplasmic N shuttling and other functions of N⁵⁰. In addition, human 14-3-3 proteins were reported to bind the mutational hotspot region of SARS-CoV-2 N and modulate SARS-CoV-2 N phosphoregulation⁵¹. In accordance with these observations, our transcriptomic data showed that PAV-104 treatment negatively regulates the maturation of nucleoprotein signaling pathway of SARS-CoV-1/2. For example, sumoylation of SARS-CoV-2 N protein can enhance its interaction affinity with itself and is critical for its nuclear translocation, which is, in turn, critical for N-mediated viral RNA genome packaging and interaction with M protein⁴¹. Phosphorylation of SARS-

CoV-2 N protein was reported to be responsible for its localization, phase-phase separation, and interaction with host factors³⁵. Moreover, our transcriptomic data showed that the assembly of inclusion bodies where viral protein modification, aggregation, and assembly occurs^{52,53}, was negatively regulated by PAV-104 treatment. The precise manner in which PAV-104 affects the post-translational modification of SARS-CoV-2 N warrants additional investigation, which may reveal antiviral mechanisms and pharmacological targets.

Our transcriptomic analysis also revealed that PAV-104 treatment of infected cells reversed SARS-CoV-2 induction of the IFN signaling pathway. IFN signaling is critical to antiviral responses^{54,55}. To counteract host defense, multiple studies have demonstrated that SARS-CoV-2 uses a multitude of mechanisms to avoid type-I IFN-mediated immune responses⁵⁶. On the other hand, robust type-I IFN responses have been associated with severe COVID-19 disease, and may exacerbate hyperinflammation during the development of severe COVID-19^{57,58}. Therefore,

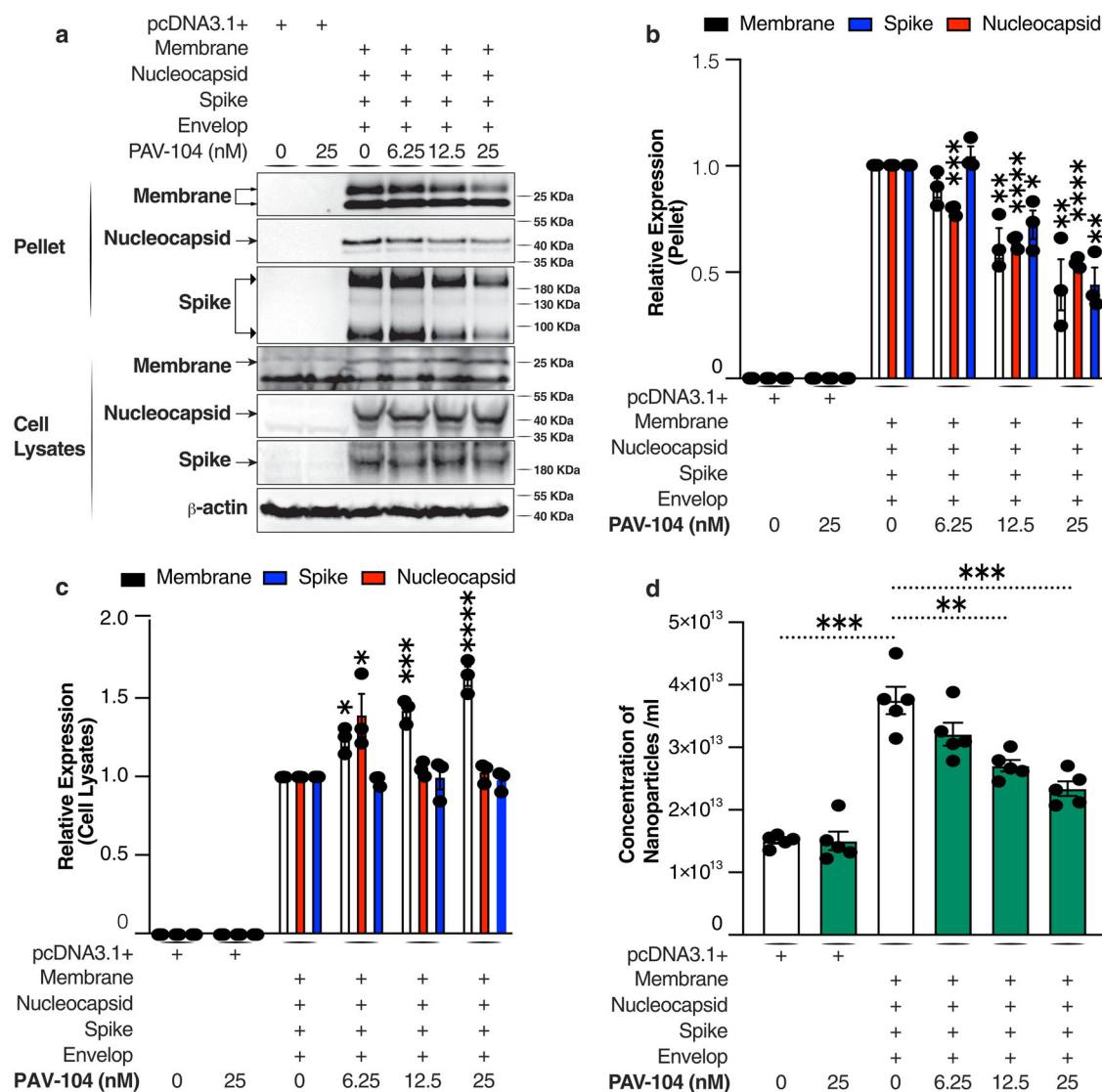


Fig. 6 | PAV-104 blocks SARS-CoV-2 virus-like particle assembly/budding. **a** Western blot analysis of structural protein expression in cell lysates and ultracentrifuged pellets. HEK293T cells were transfected with plasmids encoding the proteins indicated at the top. Western blots were performed with the primary antibodies indicated on the left of the blots. Anti- β -actin antibody was used as a loading control. **b, c** Relative quantification of the indicated protein from western blot (**a**). β -actin was used as a loading control for cell lysates and pellets. The loading control was measured on the same blot (after stripping) alongside the other proteins

in the experiment. **d** Quantification of SARS-CoV-2 VLPs by nanoparticle tracking analysis. HEK293T cells were transfected with plasmids encoding the proteins indicated at the top. VLPs containing nanoparticles in the ultracentrifuged pellets from cell culture supernatants were diluted to a concentration in the range of 10^7 – 10^9 /ml and examined using a NanoSight NS300 (NanoSight, Ltd) equipped with a 405 nm laser. $n = 5$ biologically independent samples. Data are representative of the results as mean \pm SEM. Statistical significance was analyzed by t test. $p \leq 0.05$ [*], $p \leq 0.01$ [**], $p \leq 0.001$ [***], $p \leq 0.0001$ [****].

beyond inhibition of viral replication, PAV-104 may exert adjunctive anti-inflammatory effects via selective suppression of IFN pathway members that enhances its clinical potential as a therapeutic for COVID-19.

In summary, our findings demonstrate that PAV-104, a host-targeted pan-respiratory virus small-molecule inhibitor, is a promising therapeutic candidate for SARS-CoV-2.

Methods

Cell lines

Human lung adenocarcinoma epithelial Calu-3 cells (ATCC, HTB-55) were cultured in Eagle’s Minimum Essential Medium (EMEM) (ATCC, 30-2003). African green monkey kidney Vero E6 cells (ATCC, CRL-1586) and human kidney HEK293T cells (ATCC, CRL-3216) were cultured in Dulbecco’s Modified Eagle’s medium (DMEM) (Thermo Fisher Scientific, 11965092). All media were supplemented with 10% fetal bovine serum (FBS, Corning, 35010CV) and 1% penicillin/streptomycin (Thermo Fisher

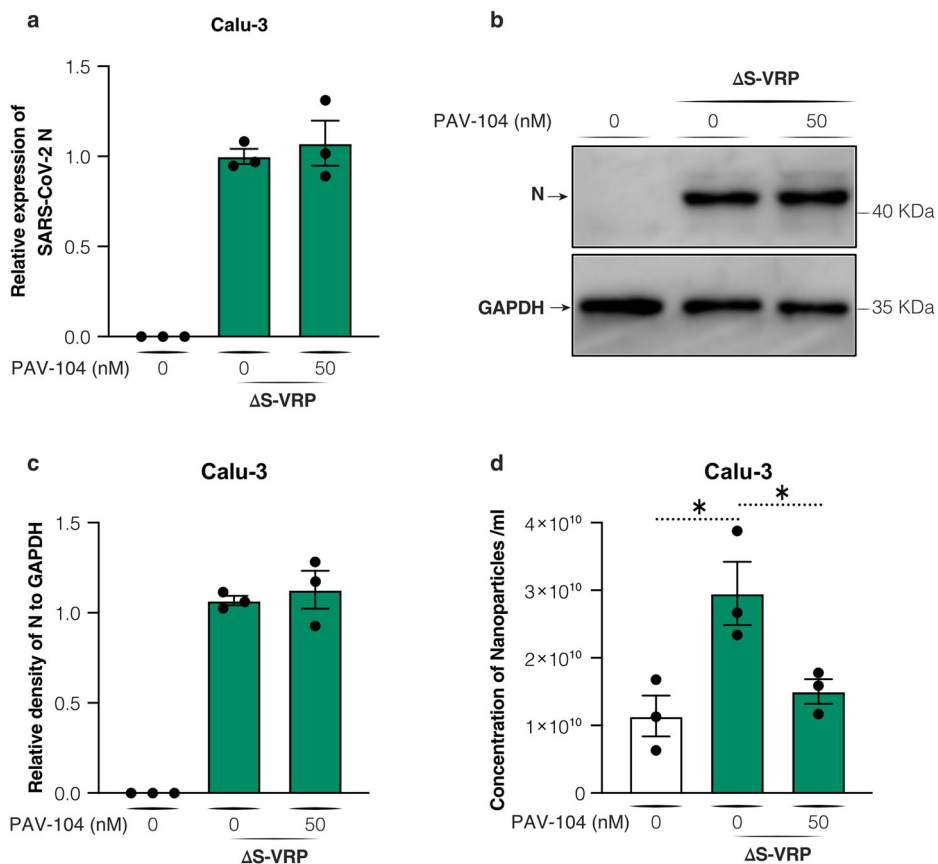
Scientific, 10378016). Vero E6 cells stably expressing TMPRSS2 (Vero E6-TMPRSS2) were established and cultured in DMEM in the presence of puromycin (1 μ g/ml) (Thermo Fisher Scientific, A1113803).

All cells had been previously tested for mycoplasma contamination and incubated at 37 $^{\circ}$ C in a humidified atmosphere with 5% CO_2 .

Primary AECs

Human unused donor tracheobronchial tissue was obtained at the time of lung transplant. The tissue was washed and placed in DMEM with 0.1% protease and antibiotics overnight at 4 $^{\circ}$ C. The next day, the solution was agitated, and the remaining tissue was removed. Cell pellets were treated with 0.05% trypsin-EDTA and then filtered through a cell strainer. Cells were plated onto 6 mm/0.4 mm Transwell ALI insert (Corning, 3470) after treatment with FNC coating mixture (Athena Enzyme Systems, 0407). 10% FBS in DMEM and ALI media were added in equal volumes to each basal compartment, and cultures were incubated at 37 $^{\circ}$ C with 5% CO_2 . The next

Fig. 7 | PAV-104 specifically inhibits SARS-CoV-2 at a late life cycle stage. **a** Nucleocapsid mRNA level of single-cycle virus Δ S-VRP in Calu-3 cells with or without PAV-104 treatment, measured by RT-qPCR. **b** Nucleocapsid (N) protein level of single-cycle virus Δ S-VRP in Calu-3 cells with or without PAV-104 treatment, measured by western blot. **c** Relative quantification of N density from western blot (**b**). GAPDH was used as a loading control. The loading control was re-probed on the same blot alongside the other proteins in the experiment. **d** Quantification of viral particles by nanoparticle tracking analysis. Data are representative of the results of three independent experiments ($n = 3$ biologically independent samples, mean \pm SEM). Statistical significance was determined by *t* test. $p \leq 0.05$ [*], $p \leq 0.01$ [**], $p \leq 0.001$ [***], $p \leq 0.0001$ [****].



day, the media was removed, and both compartments were washed with PBS and antibiotics. ALI media was then added to each basal compartment and changed every three days for at least 28 days until differentiated airways were ready for use²⁹.

Viruses

The severe acute respiratory syndrome coronavirus-2 (SARS-CoV-2) strains USA-WA1/2022, lineage P.1 (Gamma), lineage B.1.617.2 (Delta), and lineage B.1.1.529 (Omicron) were obtained from BEI Resources of the National Institute of Allergy and Infectious Diseases (NIAID) and propagated in Vero E6-TMPRSS2 cells. Virus titer was measured in Vero E6 cells by TCID₅₀ assay. All the studies involving live viruses were conducted in the Vitalant Research Institute BSL-3 under approved safety protocols.

Ethics statement

The studies involving human participants were reviewed and approved by the Human Research Protection Program, University of California, San Francisco. The patients/participants provided their written informed consent to participate in this study. All ethical regulations relevant to human research participants were followed.

Drug cytotoxicity assay

The cytotoxic effect of PAV-104 on Calu-3 cells was measured using an MTT assay kit (Abcam, ab211091) following the manufacturer's instructions. In brief, Calu-3 cells were seeded in 96-well cell culture plates. Appropriate concentrations of PAV-104 were added to the medium (0–5000 nM). After 48 h, the media was removed, and 100 μ l MTT reagent (1:1 dilution in DMEM medium (serum-free)) was added to each well and incubated for 3 h at 37 $^{\circ}$ C. Then the medium was removed, and 150 μ l MTT solvent was added to each well. Quantification was performed by reading absorbance at OD = 590 nm. The data from three independent experiments was used to calculate the CC₅₀ by nonlinear regression using GraphPad Prism 8.0 software.

SARS-CoV-2 infection and drug administration

Calu-3 cells were seeded at 0.5×10^6 cells per well in 0.5 ml volumes using a 24-well plate, or were seeded at 1×10^5 cells per well in 0.1 ml volumes using a 96-well plate. The following day, cells were pretreated with or without PAV-104 or remdesivir (SIGMA, 1809249-37-3) for one hour. Then viral inoculum (MOI of 0.01; 500 μ l/well or 100 μ l/well) was prepared using EMEM containing indicated concentrations of PAV-104 or remdesivir and added to the wells. The inoculated plates were incubated at 37 $^{\circ}$ C with 5% CO₂. At indicated infection time points, supernatants were collected and stored at -80° C. Cells were lysed with TRizol (Thermo Fisher Scientific, 15596026) for RNA extraction.

For infection of primary AECs in ALI culture, cells were pretreated with PAV-104 in the basal compartment for one hour. SARS-CoV-2 (diluted in ALI-culture medium, MOI = 0.1) was added to the apical chamber of inserts (250 μ l) and the basal compartment (500 μ l). Then the cultures were incubated for 2 h at 37 $^{\circ}$ C (5% CO₂) to enable virus entry. Subsequently, the cells were washed, and fresh ALI medium (500 μ l) containing PAV-104 was added into the basal compartment. Cells were incubated at 37 $^{\circ}$ C (5% CO₂) and harvested for analysis at 36 h post infection.

Δ S-VRP infection and drug administration

Stocks of Δ S-VRP were prepared by Dr. Manicassamy Lab⁵⁹. Calu-3 cells were seeded at 1×10^6 cells per well in 1 mL volumes using a 12-well plate. The following day, cells were pretreated with or without PAV-104 for one hour. Then the viral inoculum (1 mL/12 wells) was prepared using EMEM containing indicated concentrations of PAV-104 and added to the wells. The inoculated plates were incubated at 37 $^{\circ}$ C with 5% CO₂ for 2 h. Cells were washed three times with PBS to remove extracellular virus, and then supplied with EMEM containing indicated concentrations of PAV-104 for another 18 h. Supernatants were collected and stored at -80° C for nanoparticle measurement. Cells were lysed with TRizol (Thermo Fisher Scientific, 15596026) for RNA extraction or lysed with RIPA (Thermo Fisher Scientific, 89900) for immunoblotting.

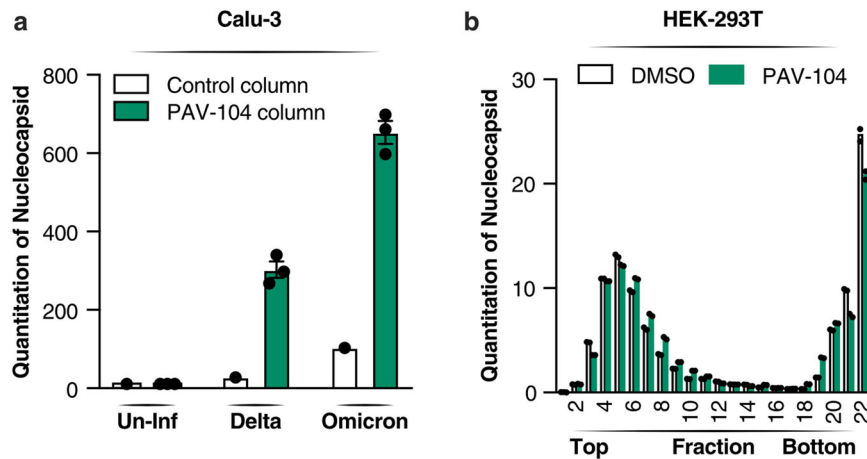


Fig. 8 | PAV-104 interacts with N and interferes with N oligomerization.
a Quantitation of resin-bound N band density detected by western blot. DRAC experiments were performed on the PAV-104 resin column in triplicate and control resin column in singlicate from cell extracts prepared from Calu-3 cells that were uninfected (Un-Inf) or infected with SARS-CoV-2 Delta variant (Delta) or SARS-CoV-2 Omicron variant (Omicron). Material bound to the PAV-104 resin was run on gels and western blot for SARS-CoV-2 N. $n = 3$ biologically independent samples. The quantitation of each fraction was normalized to the total N protein

quantity. Data are representative of the results as mean \pm SEM. Statistical significance was analyzed by t test. $p \leq 0.05$ [*], $p \leq 0.01$ [**], $p \leq 0.001$ [***], $p \leq 0.0001$ [****]. **b** Quantitation of SARS-CoV-2 N in each fraction. Cell extracts from N-transfected cells in the presence or absence of PAV-104 were sedimented in a 10–40% glycerol gradient at $135,000 \times g$ for 20 h. Twenty-two fractions were collected, and protein content analyzed using a commercial SARS-CoV-2 N protein sandwich ELISA kit (duplicate). $n = 2$ biologically independent samples.

Viral titer by TCID₅₀ assay

Virus production in the supernatant was measured by quantifying TCID₅₀. Vero E6 cells were plated in 96-well plates at 5×10^4 cells per well. The next day, supernatants collected from Calu-3 cells were subjected to 10-fold serial dilutions (10^1 – 10^{11}) and inoculated onto Vero E6 cells. The cells were incubated at 37 °C with 5% CO₂. Three to five days post infection, each inoculated well was evaluated for the presence or absence of viral CPE. TCID₅₀ was calculated based on the method of Reed and Muench⁶⁰.

RT-qPCR

Total RNA was extracted using TRIzol reagent according to the manufacturer's instructions. Reverse transcription was performed using RevertAid First Strand cDNA Synthesis Kit (Thermo Fisher Scientific, K1622) in accordance with the manufacturer's instructions. RT-qPCR was performed for each sample using Taqman Universal Master mix II, with UNG (Thermo Fisher Scientific, 4440038) on a ViiA7 Real-time PCR system. Primers and probes for detection of the *RNaseP* gene and SARS-CoV-2 *nucleocapsid* (N) gene were obtained from IDT (2019-nCoV RUO Kit (Integrated DNA Technologies, 10006713)). The expression level of the N gene was determined relative to the endogenous control of the cellular *RNaseP* gene.

RNA-sequencing analysis

RNA concentration and quality were measured using High Sensitivity RNA ScreenTape Analysis (Agilent, 5067-1500). cDNA libraries were constructed and sequencing was performed by Novogene using their mRNA sequencing protocol. The raw RNA-sequencing data were aligned to the human genome (GRCh38) using STAR (version 2.7.3a). Donor effects were removed using the “removeBatchEffect” limma package, implemented in the R computing environment (Supplementary Fig. 4)⁶¹. Analysis of differential expression was performed using DESeq2 according to a standard protocol. Genes with adjusted P value < 0.05 were considered as significantly differentially expressed. GSEA was performed using the fgsea package (version 1.22.0) in R. Enrichment of GO biological process terms in cluster genes from each module was tested using a hypergeometric test in the clusterProfiler package (v4.10.0) with the Bonferroni procedure. Terms enriched with an adjusted p value < 0.05 were considered significant. The Reactome database (version 7.5.1) was downloaded from MSigDB (<https://www.gsea-msigdb.org>).

Immunofluorescence microscopy and image analysis

Cells were fixed and permeabilized with cold methanol:acetone (1:1) for 10 min at 4 °C according to our previous method²⁹. In brief, cells were washed with 1 \times PBS and incubated in a blocking buffer (5% goat serum, Seracare Life Sciences Inc, 55600007) at room temperature for 30 min. Cells were then incubated with a primary antibody (monoclonal rabbit anti-SARS-CoV-2 N antibody, GeneTex, GTX135357) in 1 \times PBS (1:1000) overnight at 4 °C. The following day, cells were washed three times with 1 \times PBS and incubated with a secondary antibody (Goat anti-Rabbit IgG (H + L) secondary antibody, FITC (Thermo Fisher, 65-6111)) in 1 \times PBS (1:200) for 1 h at 37 °C. Then cells were washed three times with 1 \times PBS and incubated with DAPI (300 nM) (Thermo Fisher Scientific, D1306) for 5 min at room temperature. Images were acquired using a fluorescence microscope (ECHO, Revolve).

To measure the frequency of infected cells, randomly-selected areas were imaged. Each treatment had three replicates. The FITC-positive cells and DAPI-positive cells were quantified using CellProfiler software (4.2.1)²⁹. The same threshold value was applied to the images of each area.

Quantification of the western blots was carried out with Image J software (1.52q). β -actin/GAPDH were used as loading controls.

Production of SARS-CoV-2 VLPs

HEK293T cells were seeded in T75 cell culture flasks. The next day, cells were transfected with empty pcDNA3.1 plasmid or pcDNA3.1 plasmid encoding the SARS-CoV-2 M (Addgene, 158078), E (Addgene, 158080), N (Addgene, 158079), and S proteins (Addgene, 158074), as indicated. 1 μ g of each plasmid was used, with 5 μ g of total plasmid in each transfection, normalized using empty vectors, in 400 μ l Opti-MEM and 18 μ l of PEI. The transfection mixture was incubated at room temperature for 15 min and dropped into the HEK293T cells. Six hours post transfection, the media was removed and supplemented with fresh medium containing PAV-104 at indicated concentrations. The supernatant and cell lysate were collected after 60 h. For the purification of SARS-CoV-2 VLPs, the supernatant was passed through a 0.45 μ m syringe filter (SIGMA, SLGVM33RS), then loaded on top of a 20% sucrose cushion in PBS, and ultracentrifuged at 30,000 rpm in an SW41 rotor for two hours. VLP-containing pellets were washed with ice cold PBS and resuspended in SDS loading buffer, followed by sonication in an ice-water bath. Or VLP-containing pellets were resuspended in PBS (passed through 0.22 μ m syringe filter (SIGMA,

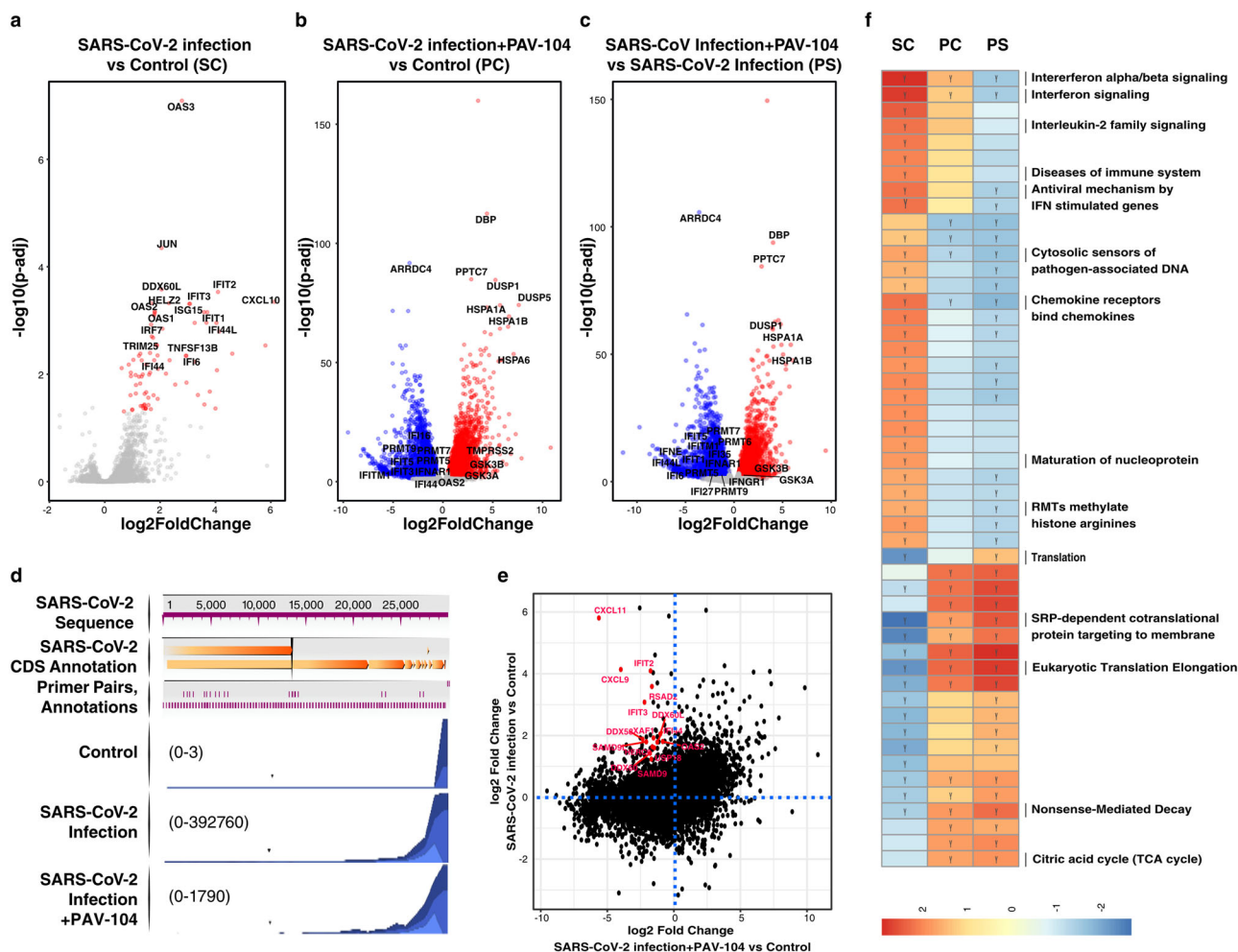


Fig. 9 | Impact of SARS-CoV-2 infection and PAV-104 treatment on the transcriptome of primary AECs. a–c Volcano plots showing the proportion of differentially expressed genes (DEGs) in the setting of SARS-CoV-2 infection (MOI = 0.1) (SARS-CoV-2 infection vs Control (SC)) (a), SARS-CoV-2 infection in the presence of PAV-104 (SARS-CoV-2 infection+PAV-104 vs Control (PC)), and SARS-CoV-2 infection in the presence of PAV-104 vs SARS-CoV-2 infection (PS). DEGs (FDR < 0.05) with log₂(fold change) > 0.5 are indicated in red. DEGs (FDR < 0.05) with log₂(fold change) < -0.5 are indicated in blue. The absolute value of Log₂(fold change) < 0.5 and non-significant DEGs are indicated in gray. **d** Sample coverage tracks from the QIAGEN genome browser depicting SARS-CoV-2 assembly. Mapped read counts of Control, SARS-CoV-2 infection, and SARS-CoV-2 infection

in the presence of PAV-104 (SARS-CoV-2 infection+PAV-104) are 0 to 3, 0 to 392,760, and 0 to 1790, respectively. **e** Scatter plot highlighting SARS-CoV-2 infection-regulated genes reversed by PAV-104. The X axis indicates the log₂ fold change between the SARS-CoV-2 infection+PAV-104 treatment group and control. The Y axis indicates that log₂ fold change between SARS-CoV-2 infection and control. Red points denote genes significantly induced by SARS-CoV-2 infection and significantly reversed by PAV-104 treatment. **f** Top enriched REACTOME pathways in response to SARS-CoV-2 infection or PAV-104 treatment identified using gene set enrichment analysis (GSEA). The orange and blue-colored bars in the bar chart indicate predicted pathway activation or predicted inhibition, respectively, based on enrichment score. Y represents FDR < 0.25.

SLGVM33RS)) for quantification by NTA. Cells were lysed in RIPA buffer (Thermo Fisher Scientific, 89900) and sonicated in an ice-water bath.

Immunoblots of SARS-CoV-2 VLPs or ΔS-VRP nucleocapsid protein

Total protein in pellet and cell lysate samples were separated by SDS-PAGE, and subsequently electro-transferred onto a supported PVDF membrane. Membranes were cut and probed for M with rabbit anti-SARS-CoV-2 M (Thermo Fisher Scientific, PA1-41160), N with rabbit anti-SARS-CoV-2 N (Rockland Immunochemicals, 200-401-A50), E with rabbit anti-SARS-CoV-2 E (Thermo Fisher Scientific, PA5-112047), and S with rabbit anti-SARS-CoV-2 S1/S2 (Thermo Fisher Scientific, PA5-112048) or with mouse anti-SARS-CoV-2 spike (Genetex Inc, GTX632604). Goat anti-rabbit IgG HRP and goat anti-mouse IgG HRP secondary antibodies were used as appropriate. β-actin was used as a cell lysate and pellet loading control by probing membranes with rabbit anti-human β-actin, conjugated with HRP (Cell Signaling Technology, 12620). All antibodies were diluted in 5% milk, and membranes were washed with Tween 20 washing buffer (Thermo

Fisher Scientific, J60304.K3). Chemiluminescent signal was visualized using SuperSignal West Femo Substrate (Thermo Fisher Scientific, PI34094) or using ECL Blotting Reagents (SIGMA, GERPN2109), and imaged using ImageQuant LAS 4000.

Quantification of VLPs by NTA

VLP-containing pellets were diluted in PBS (passed through 0.22 μm syringe filter) to a concentration in the range of 10⁷–10⁹/ml and examined using a NanoSight NS300 (NanoSight Ltd) equipped with a 405 nm laser. Five 60 s-long videos were taken for each sample with camera level 16 and the detection threshold set at 5. Raw data of particle movement and laser scattering were analyzed using NTA software (version 3.3, NanoSight Ltd). The output data were presented as nanoparticle concentration and size.

Drug resin affinity chromatography

DRAC experiments were performed where 30 μl of extract prepared from Calu-3 cells under different infection and treatment conditions were

adjusted to a protein concentration of ~2.3 mg/ml in column buffer (50 mM HEPES, pH 7.6, 100 nM KAc, 6 mM MgAc, 1 mM EDTA, and 4 mM TGA) and supplemented with an “energy cocktail” (to a final concentration of 1 mM rATP, 1 mM rGTP, 1 mM rCTP, 1 mM UTP, 4 mM creatine phosphate, pH 7.6) and 5 µg/mL creatine kinase and incubated on a column containing 30 µl of Affi-gel resin (BIO-RAD, 1536099) coupled to either PAV-104 or a 4% agarose matrix (control) for one hour at room temperature. The PAV-104 resin conditions were run side-by-side in triplicate, while the control resin conditions were done in single point. The flow-through material was collected, and the resin was washed with 1.5 mL column buffer then eluted with 100 µl PAV-104 plus the energy cocktail at room temperature for 2 hours, then stripped with 100 µl 1% SDS. The eluate and SDS-stripped material run on agarose gels and are analyzed by western blot for SARS-CoV-2 N protein (Rockland Immunochemicals, 200-401-A50).

Glycerol gradient sedimentation and ELISA-based assessment of SARS-CoV-2 N

Cell extracts from SARS-CoV-2 N-transfected HEK-293T cells in the presence or absence of PAV-104 were centrifuged at $15,000 \times g$ for 10 min at 4 °C to obtain the supernatant. 200 µl of supernatant were loaded on the top of a 5 ml continuous 10–40% glycerol gradient in lysis buffer (v/v, Pierce IP Lysis Buffer (Thermo Fisher, 87787)) prepared using the Gradient Master machine (Biotcomp, Gradient Station). After concentration at $135,000 \times g$ for 20 h at 4 °C in a SW55 rotor (Beckman Coulter), 22 fractions of 250 µl were collected from the top to the bottom of the gradient.

Proteins were assessed by the commercial SARS-CoV-2 N protein sandwich ELISA kit (GeneTex, GTX535824) following the manufacturer’s instructions. In brief, each fraction was diluted to 1:1000 using an assay dilute reagent. 50 µl of each standard and samples were added into the appropriate wells, then incubated at room temperature for 2 h. The solutions in the wells were aspirated, and the wells were washed with a washing buffer six times. Then the conjugate solution was added and incubated at room temperature for 1 h. The solutions in the wells were aspirated, and the wells were washed with a washing buffer six times once again. TMB solution was added to the wells and incubated in darkness for 15 min at room temperature. A stop solution was added to each well. Finally, optical density at 450 nm was read within 15 min.

Statistics and reproducibility

Statistical analysis was performed using GraphPad Prism version 8 software. Sample sizes are indicated in the figure legends. Data were collected from a minimum of three independent experiments, with the exception of the data describing nucleocapsid concentrations detected by ELISA, which were obtained from two independent experiments. Data were presented as means ± SEM or median. Data were analyzed for statistical significance using an unpaired or paired Student’s *t* test to compare two groups, or using a paired *t* test. Only *p* values of 0.05 or lower were considered statistically significant (*p* > 0.05 [ns], *p* ≤ 0.05 [*], *p* ≤ 0.01 [**], *p* ≤ 0.001 [***], *p* ≤ 0.0001 [****]).

Reporting summary

Further information on research design is available in the Nature Portfolio Reporting Summary linked to this article.

Data availability

The DEG lists are shown in Supplementary Data 1–3. The GSEA pathway enrichment data are shown in Supplementary Data 4. Sequencing data are available in the NCBI Gene Expression Omnibus under the GEO accession number GSE261002. All of the data generated or analyzed during this study are included in this published article or are available from the corresponding author upon reasonable request. The source data underlying the graphs in the figure are shown in Supplementary Data 5. Supplementary Figs. 5–13 contain the original uncropped blot images associated with the main figures.

Code availability

Source codes and accompanying information can be found at <https://github.com/ldu1/PAV104.git>.

Received: 5 May 2023; Accepted: 1 April 2024;

Published online: 22 April 2024

References

- Hu, B., Guo, H., Zhou, P. & Shi, Z.-L. Characteristics of SARS-CoV-2 and COVID-19. *Nat. Rev. Microbiol.* **19**, 141–154 (2021).
- Razonable, R. R. et al. Casirivimab–Imdevimab treatment is associated with reduced rates of hospitalization among high-risk patients with mild to moderate coronavirus disease-19. *eClinicalMedicine* **40**, 101102 (2021).
- Thilagar, B. P. et al. Anti-spike monoclonal antibody therapy in pregnant women with mild-to-moderate coronavirus disease 2019 (COVID-19). *Obstet. Gynecol.* **139**, 616–618 (2022).
- Chen, R. E. et al. In vivo monoclonal antibody efficacy against SARS-CoV-2 variant strains. *Nature* **596**, 103–108 (2021).
- Beigel, J. H. et al. Remdesivir for the treatment of Covid-19 - final report. *N. Engl. J. Med.* **383**, 1813–1826 (2020).
- Jayk Bernal, A. et al. Molnupiravir for oral treatment of Covid-19 in nonhospitalized patients. *N. Engl. J. Med.* **386**, 509–520 (2022).
- Owen, D. R. et al. An oral SARS-CoV-2 Mpro inhibitor clinical candidate for the treatment of COVID-19. *Science* **374**, 1586–1593 (2021).
- Wang, Y. et al. Remdesivir in adults with severe COVID-19: a randomised, double-blind, placebo-controlled, multicentre trial. *Lancet* **395**, 1569–1578 (2020).
- Miranda, J. A., McKinzie, P. B., Dobrovolsky, V. N. & Revollo, J. R. Evaluation of the mutagenic effects of Molnupiravir and N4-hydroxycytidine in bacterial and mammalian cells by HiFi sequencing. *Environ. Mol. Mutagen* **63**, 320–328 (2022).
- Zhou, S. et al. β-d-N4-hydroxycytidine inhibits SARS-CoV-2 through lethal mutagenesis but is also mutagenic to mammalian cells. *J. Infect. Dis.* **224**, 415–419 (2021).
- Wang, L. et al. COVID-19 rebound after paxlovid and molnupiravir during January–June 2022. *medRxiv* <https://doi.org/10.1101/2022.06.21.22276724> (2022).
- Hashimoto, R. et al. Dual inhibition of TMPRSS2 and Cathepsin B prevents SARS-CoV-2 infection in iPSC cells. *Mol. Ther. Nucleic Acids* **26**, 1107–1114 (2021).
- Zhang, Q. et al. Molecular mechanism of interaction between SARS-CoV-2 and host cells and interventional therapy. *Sig. Transduct. Target Ther.* **6**, 1–19 (2021).
- Mengist, H. M., Dilnessa, T. & Jin, T. Structural basis of potential inhibitors targeting SARS-CoV-2 main protease. *Front. Chem.* **9**, 622898 (2021).
- Narayanan, A. et al. Identification of SARS-CoV-2 inhibitors targeting Mpro and PLpro using in-cell-protease assay. *Commun. Biol.* **5**, 169 (2022).
- Ahamad, S., Gupta, D. & Kumar, V. Targeting SARS-CoV-2 nucleocapsid oligomerization: insights from molecular docking and molecular dynamics simulations. *J. Biomol. Struct. Dyn.* **40**, 2430–2443 (2022).
- Cai, T., Yu, Z., Wang, Z., Liang, C. & Richard, S. Arginine methylation of SARS-Cov-2 nucleocapsid protein regulates RNA binding, its ability to suppress stress granule formation, and viral replication. *J. Biol. Chem.* **297**, 100821 (2021).
- Bhowmik, D. et al. Identification of potential inhibitors against SARS-CoV-2 by targeting proteins responsible for envelope formation and virion assembly using docking based virtual screening, and pharmacokinetics approaches. *Infect. Genet. Evol.* **84**, 104451 (2020).

19. He, R. et al. Characterization of protein–protein interactions between the nucleocapsid protein and membrane protein of the SARS coronavirus. *Virus Res.* **105**, 121–125 (2004).
20. Khambhati, K. et al. Exploring the potential of cell-free protein synthesis for extending the abilities of biological systems. *Front. Bioeng. Biotechnol.* **7**, 248 (2019).
21. Rodríguez-Limas, W. A., Sekar, K. & Tyo, K. E. J. Virus-like particles: the future of microbial factories and cell-free systems as platforms for vaccine development. *Curr. Opin. Biotechnol.* **24**, 1089–1093 (2013).
22. Spice, A. J., Aw, R., Bracewell, D. G. & Polizzi, K. M. Synthesis and assembly of hepatitis B virus-like particles in a pichia pastoris cell-free system. *Front. Bioeng. Biotechnol.* **8**, 72 (2020).
23. Lingappa, U. F. et al. Host–rabies virus protein–protein interactions as druggable antiviral targets. *Proc. Natl. Acad. Sci.* **110**, E861–E868 (2013).
24. Müller-Schiffmann, A. et al. A pan-respiratory antiviral chemotype targeting a transient host multiprotein complex. Preprint at <https://doi.org/10.1101/2021.01.17.426875> (2022).
25. Reed, J. C. et al. Identification of an antiretroviral small molecule that appears to be a host-targeting inhibitor of HIV-1 assembly. *J. Virol.* **95**, e00883–20 (2021).
26. Grein, J. et al. Compassionate use of remdesivir for patients with severe Covid-19. *N. Engl. J. Med.* **382**, 2327–2336 (2020).
27. Pruijssers, A. J. et al. Remdesivir inhibits SARS-CoV-2 in human lung cells and chimeric SARS-CoV expressing the SARS-CoV-2 RNA polymerase in mice. *Cell Rep.* **32**, 107940 (2020).
28. Ryu, G. & Shin, H.-W. SARS-CoV-2 infection of airway epithelial cells. *Immune Netw.* **21**, e3 (2021).
29. Du, L. et al. Human galectin-9 potently enhances SARS-CoV-2 Replication and inflammation in airway epithelial cells. *J. Mol. Cell. Biol.* **15**, mjad030 (2023).
30. Cheng, Y.-W. et al. Furin inhibitors block SARS-CoV-2 spike protein cleavage to suppress virus production and cytopathic effects. *Cell Rep.* **33**, 108254 (2020).
31. Sasaki, M. et al. S-217622, a SARS-CoV-2 main protease inhibitor, decreases viral load and ameliorates COVID-19 severity in hamsters. *Sci. Transl. Med.* **15**, eabq4064 (2022).
32. Marín-Palma, D. et al. Curcumin inhibits in vitro SARS-CoV-2 infection in vero E6 cells through multiple antiviral mechanisms. *Molecules* **26**, 6900 (2021).
33. Plescia, C. B. et al. SARS-CoV-2 viral budding and entry can be modeled using BSL-2 level virus-like particles. *J. Biol. Chem.* **296**, 100103 (2021).
34. Yurkovetskiy, L. et al. Structural and functional analysis of the D614G SARS-CoV-2 spike protein variant. *Cell* **183**, 739–751.e8 (2020).
35. Lu, S. et al. The SARS-CoV-2 nucleocapsid phosphoprotein forms mutually exclusive condensates with RNA and the membrane-associated M protein. *Nat. Commun.* **12**, 502 (2021).
36. Cong, Y., Kriegenburg, F., de Haan, C. A. M. & Reggiori, F. Coronavirus nucleocapsid proteins assemble constitutively in high molecular oligomers. *Sci. Rep.* **7**, 5740 (2017).
37. Wu, C. et al. Characterization of SARS-CoV-2 N protein reveals multiple functional consequences of the C-terminal domain. *bioRxiv* <https://doi.org/10.1101/2020.11.30.404905> (2020).
38. Scherer, K. M. et al. SARS-CoV-2 nucleocapsid protein adheres to replication organelles before viral assembly at the Golgi/ERGIC and lysosome-mediated egress. *Sci. Adv.* **8**, eabl4895 (2022).
39. Cubuk, J. et al. The SARS-CoV-2 nucleocapsid protein is dynamic, disordered, and phase separates with RNA. *Nat. Commun.* **12**, 1936 (2021).
40. Grunewald, M. E., Fehr, A. R., Athmer, J. & Perlman, S. The coronavirus nucleocapsid protein is ADP-ribosylated. *Virology* **517**, 62–68 (2018).
41. Li, F. Q., Xiao, H., Tam, J. P. & Liu, D. X. Sumoylation of the nucleocapsid protein of severe acute respiratory syndrome coronavirus. *FEBS Lett.* **579**, 2387–2396 (2005).
42. Madahar, V. et al. Human post-translational SUMOylation modification of SARS-CoV-2 nucleocapsid protein enhances its interaction affinity with itself and plays a critical role in its nuclear translocation. *Viruses* **15**, 1600 (2023).
43. Yaron, T. M. et al. Host protein kinases required for SARS-CoV-2 nucleocapsid phosphorylation and viral replication. *Sci. Signal.* **15**, eabm0808 (2022).
44. Yang, Z. et al. Interaction between host G3BP and viral nucleocapsid protein regulates SARS-CoV-2 replication. *bioRxiv* <https://doi.org/10.1101/2023.06.29.546885> (2023).
45. Ye, Q., West, A. M. V., Silletti, S. & Corbett, K. D. Architecture and self-assembly of the SARS-CoV-2 nucleocapsid protein. *Protein Sci.* **29**, 1890–1901 (2020).
46. McBride, R., van Zyl, M. & Fielding, B. C. The coronavirus nucleocapsid is a multifunctional protein. *Viruses* **6**, 2991–3018 (2014).
47. Carnes, S. K., Sheehan, J. H. & Aiken, C. Inhibitors of the HIV-1 capsid, a target of opportunity. *Curr. Opin. HIV AIDS* **13**, 359–365 (2018).
48. Gordon, D. E. et al. A SARS-CoV-2 protein interaction map reveals targets for drug repurposing. *Nature* **583**, 459–468 (2020).
49. Zhou, Y. et al. A comprehensive SARS-CoV-2–human protein–protein interactome reveals COVID-19 pathobiology and potential host therapeutic targets. *Nat. Biotechnol.* **41**, 128–139 (2023).
50. Surjit, M. et al. The severe acute respiratory syndrome coronavirus nucleocapsid protein is phosphorylated and localizes in the cytoplasm by 14-3-3-mediated translocation. *J. Virol.* **79**, 11476–11486 (2005).
51. Tugaeva, K. V. et al. Human 14-3-3 proteins site-selectively bind the mutational hotspot region of SARS-CoV-2 nucleoprotein modulating its phosphoregulation. *J. Mol. Biol.* **435**, 167891 (2023).
52. Hoenen, T. et al. Inclusion bodies are a site of ebolavirus replication. *J. Virol.* **86**, 11779–11788 (2012).
53. Zhu, N. et al. Morphogenesis and cytopathic effect of SARS-CoV-2 infection in human airway epithelial cells. *Nat. Commun.* **11**, 3910 (2020).
54. Diamond, M. S. & Kanneganti, T.-D. Innate immunity: the first line of defense against SARS-CoV-2. *Nat. Immunol.* **23**, 165–176 (2022).
55. Kim, Y.-M. & Shin, E.-C. Type I and III interferon responses in SARS-CoV-2 infection. *Exp. Mol. Med.* **53**, 750–760 (2021).
56. Gu, W. et al. The molecular mechanism of SARS-CoV-2 evading host antiviral innate immunity. *Virol. J.* **19**, 49 (2022).
57. Akamatsu, M. A., de Castro, J. T., Takano, C. Y. & Ho, P. L. Off balance: interferons in COVID-19 lung infections. *EBioMedicine* **73**, 103642 (2021).
58. Hadjadj, J. et al. Impaired type I interferon activity and inflammatory responses in severe COVID-19 patients. *Science* **369**, 718–724 (2020).
59. Malicoat, J. et al. Development of a single-cycle infectious SARS-CoV-2 virus replicon particle system for use in biosafety level 2 laboratories. *J. Virol.* **96**, e0183721 (2022).
60. Reed, L. J. & Muench, H. A simple method of estimating fifty per cent endpoints. *Am. J. Epidemiol.* **27**, 493–497 (1938).
61. Smyth, G. K. Linear models and empirical bayes methods for assessing differential expression in microarray experiments. *Stat. Appl. Genet. Mol. Biol.* **3**, Article3 (2004).

Acknowledgements

This study was supported by The Sandler Program for Breakthrough Biomedical Research (UCSF PBBR) and NIH grant R01MH112457 (to S.K.P.); Veterans Affairs Office of Research and Development CX002011

and NIH R01HL151552 (to J.R.G.). V.R.L., S.S., L.D., and S.K.P. received funding from NIH AViDD grant 1U19 AI171443; V.R.L. and S.S. received funding from Prosetta Biosciences, Inc.

Author contributions

L.D. and S.P. initiated the project and designed the experiments. L.D., F.D. and J.G. performed and processed RNA-seq. F.D. and J.G. isolated and prepared ALI-cultured primary AECs. L.D., M.B. and G.S. performed MTT and glycerol gradient sedimentation assay. J.B. analyzed RNA-seq data. L.D. and P.D. quantified VLPs by NTA. G.S. performed SARS-CoV-2 stock. B.M. generated Δ S-VRP stocks. S.S., A.L., M.M., S.Y., K.P., V.L. and H.B. prepared PAV-104 and performed the DRAC assay. L.D., V.L. and S.P. prepared the manuscript. J.G. and S.P. jointly supervised the work.

Competing interests

S.S., A.F.L., M.M., S.F.Y. and K.P. are employees of Prosetta Biosciences. V.R.L. is the CEO of Prosetta Biosciences, which manufactures PAV-104 presented in the manuscript. All other authors declare no competing interests.

Additional information

Supplementary information The online version contains supplementary material available at <https://doi.org/10.1038/s42003-024-06130-8>.

Correspondence and requests for materials should be addressed to Satish K. Pillai.

Peer review information *Communications Biology* thanks Thomas Gramberg and the other, anonymous, reviewer(s) for their contribution to the peer review of this work. Primary Handling Editors: Caroline Goujon and David Favero.

Reprints and permissions information is available at <http://www.nature.com/reprints>

Publisher's note Springer Nature remains neutral with regard to jurisdictional claims in published maps and institutional affiliations.

Open Access This article is licensed under a Creative Commons Attribution 4.0 International License, which permits use, sharing, adaptation, distribution and reproduction in any medium or format, as long as you give appropriate credit to the original author(s) and the source, provide a link to the Creative Commons licence, and indicate if changes were made. The images or other third party material in this article are included in the article's Creative Commons licence, unless indicated otherwise in a credit line to the material. If material is not included in the article's Creative Commons licence and your intended use is not permitted by statutory regulation or exceeds the permitted use, you will need to obtain permission directly from the copyright holder. To view a copy of this licence, visit <http://creativecommons.org/licenses/by/4.0/>.

© The Author(s) 2024